Superior high-frequency performances of Fe-based soft-magnetic nanocrystalline alloys

M. Jiang [a, c], M. Cai [a, c], J. Zhou [b], S. Di [a], X. Li [b], Q. Luo [a, *], B. Shen [a, **]

[a] School of Materials Science and Engineering, Jiangsu Key Laboratory for Advanced Metallic Materials, Southeast University, Nanjing 211189, PR China
[b] Songshan Lake Materials Laboratory, Dongguan 523808, PR China

ARTICLE INFO

ABSTRACT

Soft-magnetic nanocrystalline alloys with ultralow power loss are strongly desired for high-frequency power electronic applications. In this work, an industrial ultrathin FINEMET alloy ($Fe_{73.5}Si_{15.5}B_7Cu_1Nb_3$) ribbon, with 14 μm in thickness, was fabricated by using a roller thermal conductivity-controlled cooling strategy coupled with a bottom blowing argon technique. A magnetic core made of the ultrathin ribbon exhibits excellent high-frequency soft-magnetic properties, with super high permeability of 48,000 at the condition of 1 A/m and 100 kHz and an ultralow core loss of 94 kW/m^3 at the condition of 0.2 T and 100 kHz. It is found that the excess loss accounts for the largest proportion in power loss, and this proportion increases with decreasing thickness. The finest grain of nanocrystals, narrowest magnetic domain width, weakest transverse field-induced anisotropy, and considerably increased electrical resistivity (188 μΩ cm) synergistically contribute to the superior soft-magnetic performances at 100 kHz of the ultrathin alloy. This work demonstrates the attractive high-frequency application prospects of ultrathin nanocrystalline alloys in power electronics and information communication due to their excellent performance and huge energy-saving effects, and provides new and comprehensive insights into the power loss of ultrathin nanocrystalline alloys.

1. Introduction

Power electronics are developing towards energy saving, high frequency, high efficiency and reduced environmental impact, which is promoted particularly by the increasing applications of third-generation wide bandgap semiconductors. This requires urgently developing soft-magnetic materials with excellent high-frequency (ranging from kHz to a few MHz) performances like low core loss and high-saturation magnetic flux density (B_s) to fully exploit the potential of SiC- and GaN-based devices [1–5]. Among different types of soft magnets, silicon steel sheets, as the most used soft-magnetic materials, have the advantages of low cost and high B_s of 1.85–2 T, but their power loss increases quickly with increasing frequency, hindering their wide applications at high frequencies [1]. Permalloy is well-known for its high permeability but has a low electrical resistivity, and is high cost. Ferrites possess

the advantage of ultralow power loss at high frequencies and thus have been widely used. Nevertheless, their low B_s ($\leq$0.6 T) due to their ferrimagnetic nature becomes a major impediment to miniaturize the passive components [6]. The FINEMET (such as $Fe_{73.5}Cu_1Nb_3Si_{13.5}B_9$) nanocrystalline alloys (NAs) developed by Yoshizawa et al. have exhibited superior overall soft-magnetic properties over Si-steel/permalloy/ferrites, and are attractive for high-frequency applications [7]. It has been reported that at 100 kHz, these alloys show a low core loss of ~174–280 kW/m^3 at 0.2 T and a high permeability of ~20,000 at 0.05 A/m [8]. This has stimulated enormous research interest both scientifically and technologically in exploring NAs with advanced soft-magnetic performances [9–15].

The magnetic softness of NAs basically originates from the considerably reduced random anisotropy by exchange interactions, which is associated with their unique amorphous-nanocrystalline nanostructure, with a correlation length much smaller than the ferromagnetic exchange length [9]. Moreover, the uniform anisotropy of NAs plays a significant role on the magnetization process and domain configuration as well [9,16]. Thus, great efforts have been made to enhance the soft-magnetic

* Corresponding author.
** Corresponding author.
   E-mail addresses: q.luo@seu.edu.cn (Q. Luo), blshen@seu.edu.cn (B. Shen).
[c] These authors contributed equally to this work.

performances of NAs through tailoring a dual-phase structure by composition design and normal annealing, on one hand, and tuning the interplay between averaged random magnetic anisotropy and induced magnetic anisotropy by stress/magnetic field annealing on the other hand [9,17−19]. Although many compositions including the famous NANOPERM (Fe−Zr−B) [5], HITPERM (Fe−Co−Zr−B−Cu) [12], and NANOMET (Fe−Si−B−P−Cu) series [13] were developed and various treatment strategies were used, only the FINEMET alloys have gained large-scale industrial commercialization [9,18]. Other NAs have shortcomings such as poor glass forming ability, high production cost, poor industry manufacturability, or narrow annealing temperature window. Furthermore, these NAs show evidently smaller permeability and larger power loss at high frequencies than the FINEMET alloys developed 34 years ago [8,18]. Therefore, it is a big challenge to break through the high-frequency magnetic performances of NAs to meet the accelerating demand of high efficiency and miniaturization of SiC- and GaN-based devices.

Here, a $Fe_{73.5}Si_{15.5}B_7Cu_1Nb_3$ magnetic core made of ultrathin ribbon with a thickness of 14 μm was prepared. Compared with the classic FINEMET alloy $Fe_{73.5}Cu_1Nb_3Si_{13.5}B_9$, the contents of Fe, Cu, and Nb were kept unchanged in the present alloy for maintaining the saturation magnetic flux density and ultrafine grain structure. The Si content was increased from 13.5% to 15.5% to further reduce the magneto-crystalline anisotropy constant and magnetostriction, so that the alloy may obtain low coercivity and high permeability without deteriorating the glass forming ability [9,11]. After the preparation of amorphous alloy (AA) ribbons, transverse magnetic field annealing was employed to induce uniaxial magnetic anisotropy and modulate the magnetic domain structure. The obtained ultrathin NA exhibits superior high-frequency soft-magnetic properties, with superhigh relative permeability (μ_r) of 48,000 at the condition of 1 A/m and 100 kHz and extremely low power loss of 94 kW/m^3 at the condition of 0.2 T and 100 kHz. It is found that excess loss (P_{ex}) dominates overall core loss (P_{cv}) at 100 kHz, and the P_{ex} to P_{cv} ratio (P_{ex}/P_{cv}) decreases with increasing ribbon thickness (91.5% and 86.9% for samples with a thicknesses of 14 and 24 μm, respectively). The superior high-frequency performance of the ultrathin sample mainly originates from the combined effects of its finest grain, thinnest domain width, smallest induced magnetic anisotropy, and considerably increased electrical resistivity (~76% increase compared to that of the conventional ribbon with 24 μm in thickness). The results of this study demonstrate a promising application of ultrathin NAs as the next-generation, high-frequency, soft-magnetic materials used in devices based on third-generation semiconductors in the fields of consumer electronics, new energy automotive, photoelectric light sources, and telecommunication.

2. Experiments

Multicomponent alloy ingots with the nominal atomic composition of $Fe_{73.5}Si_{15.5}B_7Cu_1Nb_3$ were prepared with industrial grade raw materials of Fe (99 wt%), Cu (99.95 wt%), Si (99.85 wt%), before alloy of Fe−B (consisting of 72 wt% Fe and 18 wt% B), and Fe−Nb (consisting of 35 wt% Fe and 65 wt% Nb), respectively. Then, these ingots were melted by using a 200 kg industrial induction melting furnace under N_2 atmosphere after vacuum pumping (to about 1 Pa). As-quenched ribbons with different thicknesses were fabricated a by planar flow casting method using different wheels. The ribbons were wound into round cores with an outer diameter of 30 mm, an inner diameter of 20 mm, and a height of 10 mm. The ribbons (corresponding cores) with a thickness of 14, 16, 18, and 24 μm are denoted as the T14, T16, T18, and T24 ribbons (cores), respectively. Magnetic field annealing was conducted by employing a vacuum tube furnace under an Argon atmosphere, and the cores

were annealed at 550 °C for 60 min under a transverse magnetic field of 800 Oe.

The microstructure of the as-quenched and annealed ribbons was characterized by X-ray diffraction (Bruker D8 ADVANCE) under Cu-Kα radiation and transmission electron microscopy (TEM, Tecnai G2 T20). Thermal properties of the as-quenched ribbons were analyzed by DSC (DSC, Netzsch 404 F3), with a heating rate of 20 °C/min. Magnetic domain patterns were observed by using magneto-optical Kerr microscope (Evico Magnetics GmbH, em-Kerr-highres). The permeability was tested by impedance analyzer (Agilent 4294A) under an applied magnetic field of 1 A/m. The core loss of round cores was measured by a B−H AC analyzer (LINKJOIN MATS-2010SD/K50) at an external magnetic field of 0.2 T. The electrical resistance measurement was performed by a conventional DC four probe method (SZJG ST2742B).

3. Results and discussion

Usually, soft NAs are produced by a single roller melt spinning technique (as illustrated in Fig. 1(a)) to get AA ribbons, followed by furnace annealing to obtain a nanocrystalline microstructure. At present, commercially available NAs usually are produced with a thicknesses in the range of 16−26 μm. The industrial production of ultrathin ribbons below 16 μm remained a challenge for a long time. To get a thinner ribbon, one should reduce the melt ejection pressure (P), the distance (D) between the crucible and roller, and orifice size, and increase the roller spread (v). All the parameters expect v have already approached their limitations to fabricate ribbons with a thickness of 16 μm in mass production. It is possible to further increase the copper roller speed, but it will cause more apparent vibration of the copper roller and considerably reduce the ribbon quality. Here, instead of controlling the parameters upon using a single roller, we adopted three copper rollers with different thermal conductivities combined with a bottom blowing argon technique (to purify alloy melts) to fabricate ribbons. Finally, the industrial production of ultrathin ribbons with a thickness of 14 μm and a high surface quality (Fig. 1(b)) was prepared by using the copper roller with the lowest thermal conductivity (λ). In contrast, only ribbons with a thickness of 16 μm (18 μm) and 24 μm can be prepared by employing the copper rollers with medium and high thermal conductivities, respectively. For subsequent annealing treatment and high-frequency property tests, the as-spun ribbons were wound automatically into toroidal cores. Fig. 1(c) and (d) present the schematic diagram of transverse field annealing (TFA) for the cores and the image of one core made with the 14 μm-thick ribbon.

Fig. 2(a) shows the DSC curves of the as-quenched AA ribbons. There are two distinguishable exothermic peaks in the DSC curve of each sample, which are corresponding to the precipitation of α-Fe (first peak) and Fe−B compounds (second peak) [10]. The onset temperatures of the first (T_{x1}) and second (T_{x2}) crystalline peaks are 529 °C and 706 °C, respectively, for all the samples. Despite almost the same T_{x1} and T_{x2}, the T14, T16, T18, and T24 samples show different crystallization enthalpy values of 1.0, 1.2, 1.2, and 1.4 kJ/mol, respectively. The decrease of the crystallization enthalpy with decreasing ribbon thickness indicates an increased degree of a structure order with decreasing thickness. This is because the T14 and T24 ribbons were produced by using the copper roller with the lowest and highest thermal conductivities, respectively, leading to the lowest cooling rate of melts for the T14 sample and the highest in the T24 sample. Thus, the T14 and T24 samples have the highest and lowest degree of the local structure order, respectively. According to the DSC results, all the cores made of ribbons with different thicknesses were annealed at 550 °C for 60 min under a transverse magnetic field to produce a nanocrystalline state with
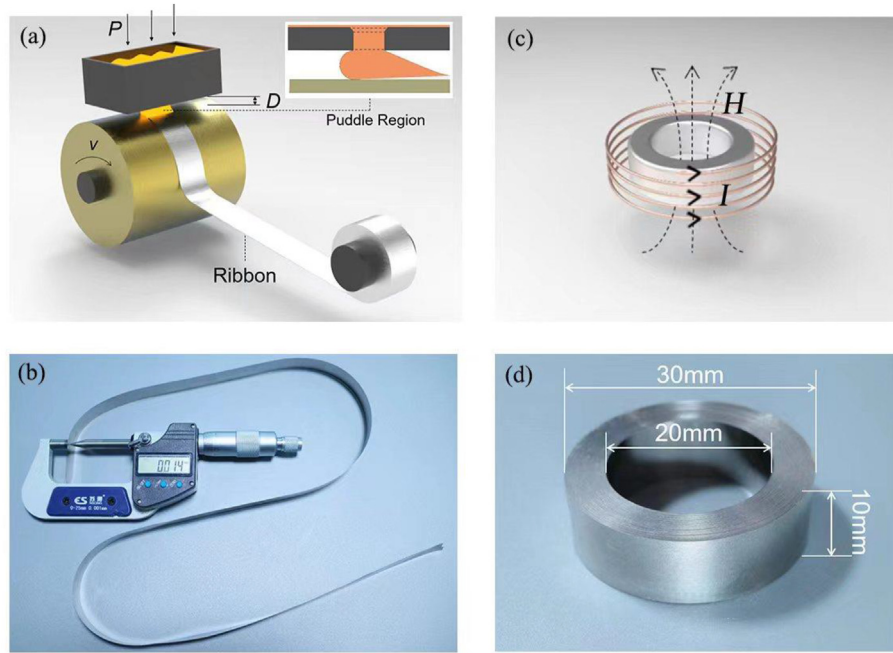
Fig. 1. (a) Schematic diagram of the planar-flow casting method, (b) photo of the as-quenched ribbon with a thickness of 14 μm, (c) schematic diagram of transverse field annealing for the cores, (d) photo of one annealed toroidal core made by using the ribbon with a thickness of 14 μm.

induced magnetic anisotropy. X-ray diffraction patterns of the annealed ribbons are shown in Fig. 2(b), which exhibit obvious crystalline peaks at $2\theta = 44.5°$, 65°, and 85°, relating to the (110) and (200) and (211) reflections of the crystalline α-Fe phase, respectively.

For the applications of NAs in high-frequency magnetic components, a combination of high permeability and low power loss is of vital importance [7,18]. The frequency dependence of the real part (μ_r) of the complex permeability of the $Fe_{73.5}Si_{15.5}B_7Cu_1Nb_3$ nanocrystalline cores with different ribbon thicknesses is illustrated in Fig. 3(a), showing a similar varying trend. That is, the permeability decreases slowly with increasing frequency between 1 and 10 kHz, through a relatively rapid drop from 10 to 100 kHz, and then varies slowly again in the highest frequency region. Importantly, obvious enhancement of the permeability with reducing thickness is observed in the whole frequency region. The T14 core exhibits the largest permeability at 1 kHz and the smallest overall degree of decay (from 1 to 100 kHz). This directly leads to a giant μ_r of 48,000 at the condition of 1 A/m and 100 kHz for the T14 core, which far exceeds those of other commercial soft-magnetic alloys used in a high-frequency region as indicated in Fig. 3(b) [7,20–22].

Fig. 4(a) shows the core loss at 0.2 T with respect to the frequency. The core loss of all the cores increases with increasing frequency and decreases significantly with decreasing thickness. The P_{cv} values at the condition of 0.2 T and 100 kHz of the T14, T16, T18, and T24 cores are 94, 114, 141, and 178 kW/m³, respectively, and their comparison is shown in the inset of Fig. 4(a). The value of 178 kW/m³ of the T24 core is comparable to other results in the conventional FINEMET alloys [7,8,23]. The reduction of power loss from 178 to 94 kW/m³, when decreasing the ribbon thickness from 24 to 14 μm, is rather impressive. Fig. 4(b) exhibits that the P_{cv} at 100 kHz of all the samples increases with increasing applied magnetic field due to the gradually increased area *swept* out by larger hysteresis loops. And a power law relation ($P_{cv} = P_0 B_m^c$, where B_m denotes the maximum flux density, P_0 and c are the fitting parameters) can fit the data very well for these samples. T14 has the

smallest exponent c of 2.1 and T24 has the largest c of 2.4 (the inset of Fig. 4(b)), indicating the slowest changing trends of the field dependences of the core loss in T14. Fig. 5 summaries the B_s and P_{cv} at the condition of 0.2 T and 100 kHz of T14 and other typical soft-magnetic materials [5,7,22,24–29], indicating the superb high-frequency performance of T14.

Then, transmission electron microscopy (TEM) examinations were conducted for the as-quenched and annealed T14, T18, and T24 samples to reveal the structural origin of their differences in high-frequency performance differences. As shown in Fig. 6(a–c), all the annealed samples show a dual-phase structure with α-Fe nanocrystalline grains embedded in the residual amorphous phase. From a statistical analysis (using more than 200 spots), the mean grain sizes of the T14, T18, and T24 samples are determined to be ~10, 12, and 14 nm, respectively (Fig. 6(d–f)), indicating the finest grains in T14. The average grain size of 10–14 nm in present samples with different thicknesses is smaller than the exchange length (20–40 nm), and their local magneto-crystalline anisotropy K_1 can thus be efficiently averaged and reduced considerably [9], rendering the magnetic softness in present samples. The finest grains in the ultrathin NA are conducive to its best soft-magnetic performance.

To illustrate the origin of grain-size differences in these samples with different thickness, high-resolution TEM images of the as-quenched amorphous samples with a thicknesses of 14 and 24 μm (Fig. 7(a and b)) are divided into 10 × 10 cells with a size of $1.915 \times 1.915 nm^2$ and then transformed into a 2D auto-correlation map (Fig. 7(c–d)) to estimate a local transitional symmetry. It is found that the T14 sample has a fraction (~15%) of the cells with a crystal-like order (red squares in Fig. 7(c)), and the T24 sample has a smaller fraction of ~10% (Fig. 7(d)). This trend is according to the DSC results showing the lowest/largest crystallization enthalpy in the T14/T24 ribbon. The larger fraction of crystal-like local structures in the as-quenched T14 ribbon is related to its lower cooling rate. This allows a longer time for atomic arrangements, promoting the formation of medium range ordered structures. The increased fraction of medium range ordered structures in the amorphous
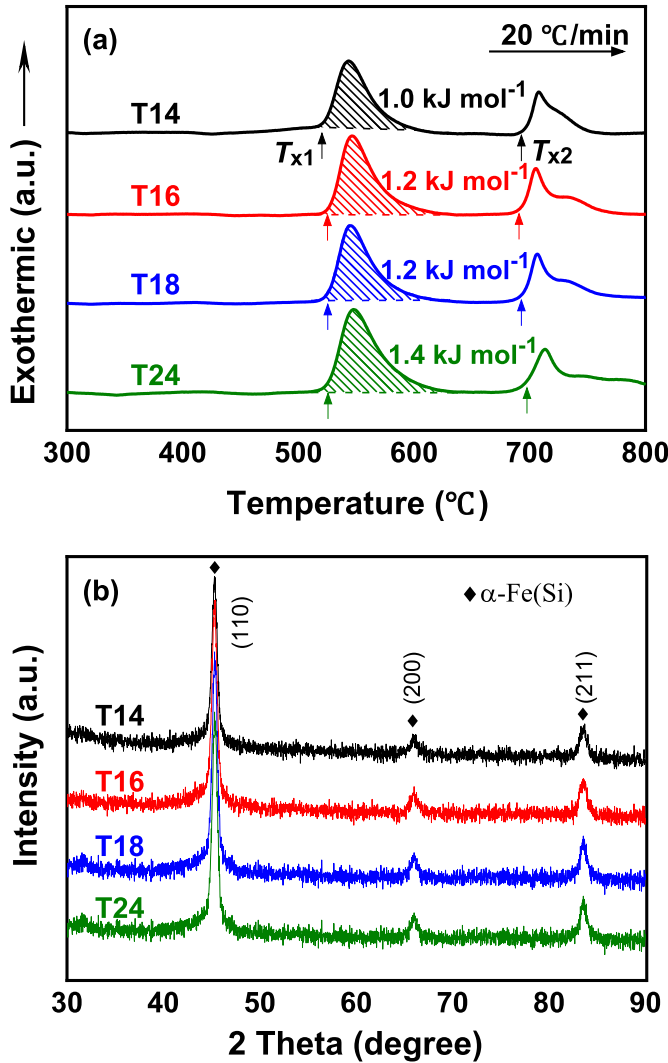
Fig. 2. (a) Differential scanning calorimetry curves of the as-quenched amorphous ribbons at a heating rate of 20 °C/min, (b) X-ray diffraction patterns of the annealed ribbons.

Fig. 3. (a) Frequency dependence of the magnetic permeability of alloy cores prepared with ribbons with different thicknesses, (b) the permeability at 100 kHz of the present T14 and other commercial alloys.

precursor can significantly block the growth of α-Fe during subsequent annealing, resulting the smallest grain size in the TFA-treated T14. Similar mechanism works in the Cu−Zr and Gd-Al-Co metallic glass systems [30,31], where the increased fraction of a local crystal-like order after minor Y or Si addition can hinder the growth of crystal-like clusters and enhance considerably the glass forming ability.

Next, we discuss the component factors of the total core loss. In terms of Bertotti's loss separation theory, the core loss in soft-magnetic alloys can be divided into hysteretic loss (P_h), classic eddy current loss (P_{ec}), and excess loss (P_{ex}) [32,33]. Usually, the hysteretic losses arising from localized Barkhausen jumps of domain walls dominate the core loss at a low frequency [32]. The eddy current loss including the classic eddy current loss and excess loss dominates at high frequencies above 10 kHz, especially for soft-magnetic NAs with an ultrafine grain structure and averaged magneto-crystalline anisotropy [34,35]. At high frequencies around 100 kHz, the hysteretic loss can be neglected due to the excellent magnetic softness in present samples. Under sinusoidal field and constant permeability, the classic eddy current losses can be evaluated by Ref. [34]:
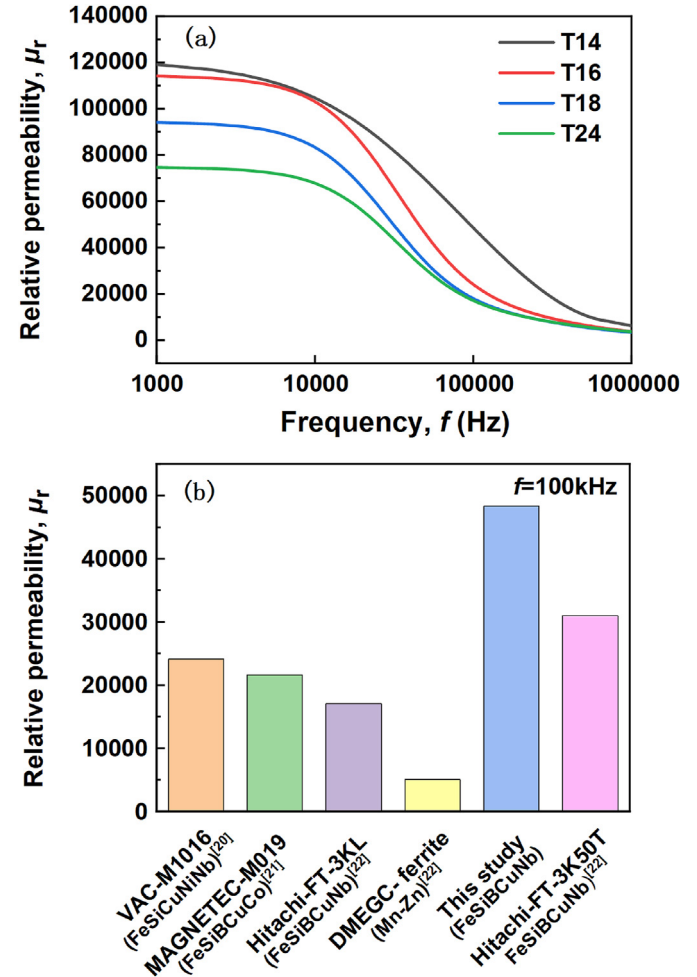
$$P_{ec} = \frac{\pi^{3/2} t B_m^2 f^{3/2}}{2\sqrt{\mu \rho_e}} \tag{1}$$

Where t is the ribbon thickness, f is the switching field frequency, u is the permeability, and ρ_e is the electrical resistivity. Eq. (1) indicates that a ribbon with thinner thickness and/or larger electrical resistivity and/or lager permeability tends to have a smaller classical eddy current loss. The ρ_e values are measured to be 188, 142, 134, and 107 μΩ cm for the T14, T16, T18, and T24 ribbons, respectively. Note that the ρ_e of 188 μΩ cm of T14 is much larger than those of other Fe-based amorphous/nanocrystalline alloy ribbons (100−130 μΩ cm) [9]. From TEM images, the volume fraction of the residual amorphous phase was determined to be 26.7%, 27.3%, and 27.6% for the T24, T18, and T14 ribbons, respectively, increasing with a decrease in the thickness [15]. It is consistent with the change of the electrical resistivity of the ribbons. However, the significant change of the electrical resistivity from 107 to 188 μΩ cm (~76% increase) with decreasing thickness from 24 to 14 μm implies that the size effect of nanocrystals play an important role. A thinner ribbon with a smaller grain size can provide more electron-scattering interfaces between nanocrystals and the residual amorphous phase, resulting in the significant increase of electrical resistivity with decreasing thickness. By using Eq. (1), the classic eddy
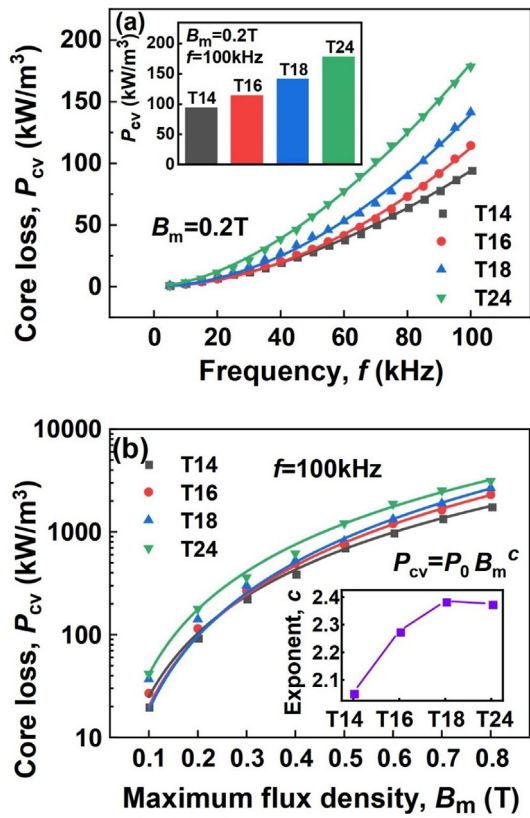
Fig. 4. (a) Frequency dependence of core loss of the alloy cores (the inset shows the core loss at 100 kHz), (b) maximum flux density dependence of the core loss at 100 kHz.
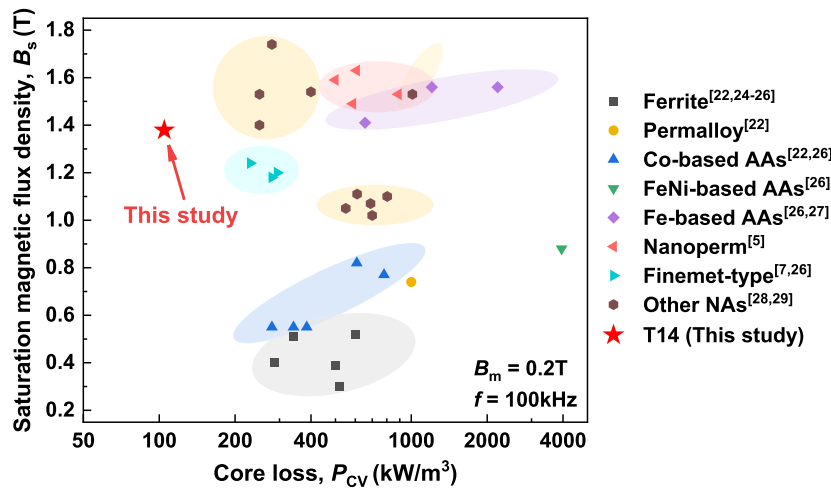
T18, and T24 cores, respectively. The ratios of the excess loss to the total core loss are 91.5%, 90.2%, 88.4%, and 86.9% of the total core loss for the T14, T16, T18 and T24 cores, respectively, which are similar to those of other NAs [34,35]. It is well-known that the excess loss arises from localized eddy current surrounding the moving domain walls under an external magnetic field. The excess loss is found to be proportional to $f^{1/2}$, owing to the increase of active domains [36,37]. In the statistical model of power loss [32], P_{ex} associates with the space-time correlation properties of the magnetization process of $n(t)$ active magnetic objects randomly placed in the sample cross section S. The excess loss can then be described by the excess field H_{ex} and number $n(t)$ of simultaneously active magnetic objects. For the case of all the switching of the magnetization taking place at a single 180° domain wall, the following relation can be obtained,

$$H_{ex} = P_{ex} / (4B_{max}f) = 4G_w SB_{max}f / \rho_e n \qquad (2)$$

Where G_w is a geometric factor and f the switching field. Eq. (2) implies that the excess loss increases with decreasing number of moving domain walls, which was observed in experimental results [36]. Considering the significance of the magnetic domain structure, static domain images in zero magnetic field of the TFA-treated T24, T18 and T14 cores were observed (the easy axis of the core is indicated by the black arrow in Fig. 8(a)) and are shown in Fig. 8(b–d). The domains of all the samples are wide and of regular shape and separated by 180° walls. This kind of a domain feature mainly arises from the modulating impact of external transverse magnetic field during annealing, and is typical in field-annealed NAs [36]. As seen from the figure, T14 shows the narrowest magnetic domain width among the three cores. The domain width cannot be accurately determined for T18 and T24 from Fig. 8 due to the limitation of the largest viewing zone.

Fig. 5. Saturation magnetic flux density (B_s) vs. core loss (P_{cv}) at 100 kHz and 0.2 T of different soft-magnetic materials including typical soft magnetic amorphous alloys and nanocrystalline alloys.

current loss at the condition of 0.2 T and 100 kHz is determined to be 8, 11, 16, and 23 kW/m³ for the T14, T16, T18, and T24 cores, respectively. As indicated in Eq. (1), the lowest classic eddy current loss of the T14 core is associated with the ultrathin thickness with the finest nanocrystalline structure, enhanced permeability, and electrical resistivity.

Moreover, the excess loss at the condition of 100 kHz and 0.2 T can be estimated to be 86,103,125, and155 kW/m³ for the T14, T16,

To further understand the magnetization process of the cores in more details, in situ observation of the magnetic domain's evolution with a varying magnetic field was performed. Fig. 9 shows the magnetic domains of T24 under different static fields. With decreasing static field from a starting field of 2.59 mT (reaching complete magnetization), black slab domains along with some drop-like domains form after around a field of 1.40 mT (Fig. 9(b)). The black domains grow further with increasing strength of the
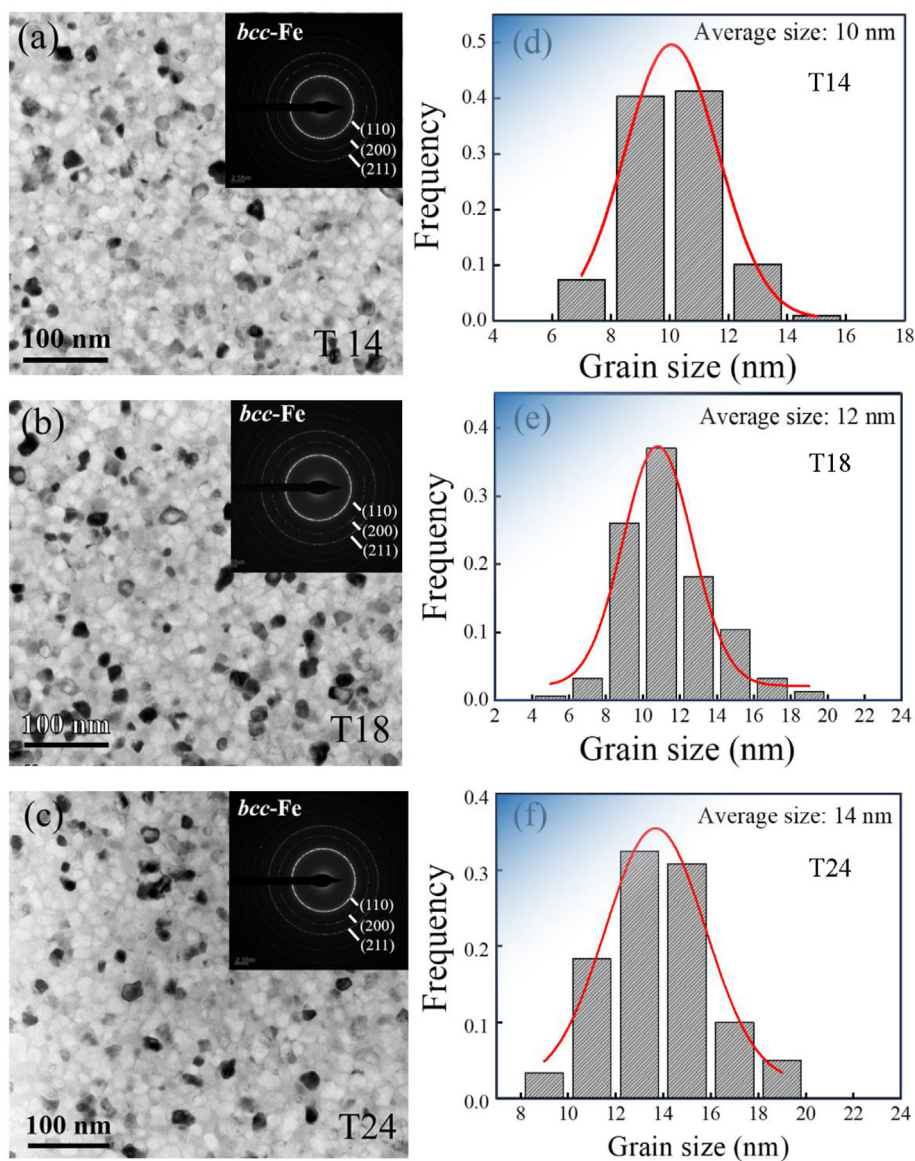
Fig. 6. (a−c) Bright-field transmission electron microscopy images and corresponding selected area electron diffraction patterns, (d−f) grain size distribution of the NA samples.

negative field ((Fig. 9(b−g)). At −2.65 mT, almost only a single black domain with one small drop-like gray domain can be observed (Fig. 9(h)). In T18 (Fig. 10(a−h)), the black slab domain develops gradually with decreasing field from 2.57 mT. And some domain splits can be detected at −0.31 mT, from which the slab-like domains begin to split into narrow stripe-like domains (Fig. 10(e−g)). Compared with T24, more stripe-like domains with a smaller width can be observed in T18 (Fig. 10(f and g)). At −2.68 mT, some narrow stripe-like gray domains are embedded in the black domains (Fig. 10(h)), which are different from those of T24 (Fig. 9(h)).

In contrast, more tiny-and-black domains appear in T14 (Fig. 11(a−d)), when the static field decreases from 2.68 mT and develop gradually into slab-like domains at 0.43 mT (Fig. 11(d)). Besides the magnetization rotation and nucleation, a clear domain splitting with branches is observed at −0.49 mT (Fig. 11(e)) and regular slab domains are observed at −0.96 mT (Fig. 11(f)). But with the further increase of the field to −2.61 mT (Fig. 11(f−h)), the inhomogeneous magnetization rotation, domain splitting and domain wall displacement lead to complicated domain patterns

with high density of the narrow stripe-like gray domains embedded in the wide black slab domains (more complicated than that of T18). The above results indicate an increase of the in-homogeneity and complexity of the magnetization process with decreasing ribbon thickness. And the highest density of the narrow stripe-like domains appears during magnetization in the thinnest T14 ribbon.

Magnetic anisotropy is the key to comprehend the magnetic domain structure and its evolution [36−39]. For the present NAs with extremely low saturation magnetostriction, the magne-toelastic anisotropy is negligible. And the external stress-induced anisotropy can be overlooked since a TFA treatment was carried out without stress. Thus, we focus on the interplay of residual random anisotropy δK ($\delta K = <K> - K_u$) and field-induced anisotropy K_u, where $<K>$ is the average anisotropy constant. From the initial magnetization curve (Fig. 12(a−c), the anisotropic field (H_k) is determined to be apparently larger than coercivity (0.42−0.48 A/ m) for the three cores, indicating the significant role of H_k on the magnetization process (as already manifested from the evolution of
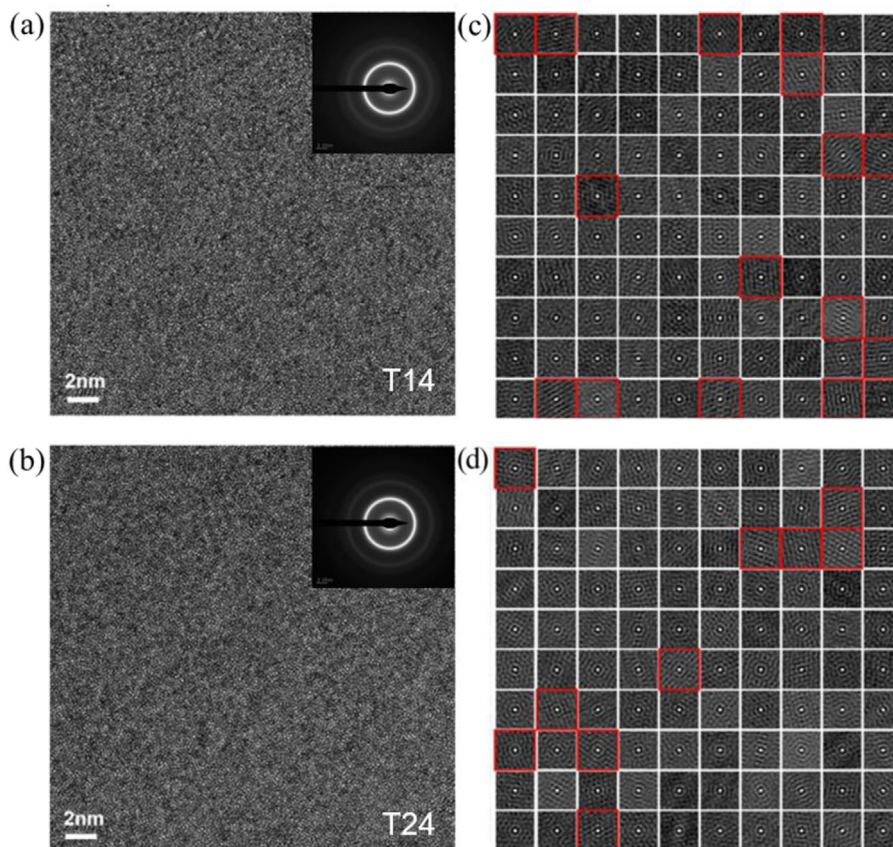
Fig. 7. High-resolution transmission electron microscopy images of the as-quenched ribbons with a thicknesses of 14 μm (a) and 24 μm (b), and the insets are the selected area electron diffraction patterns; (c) and (d) the segmentation of the selected squares in (a) and (b) for an auto-correlation analysis.
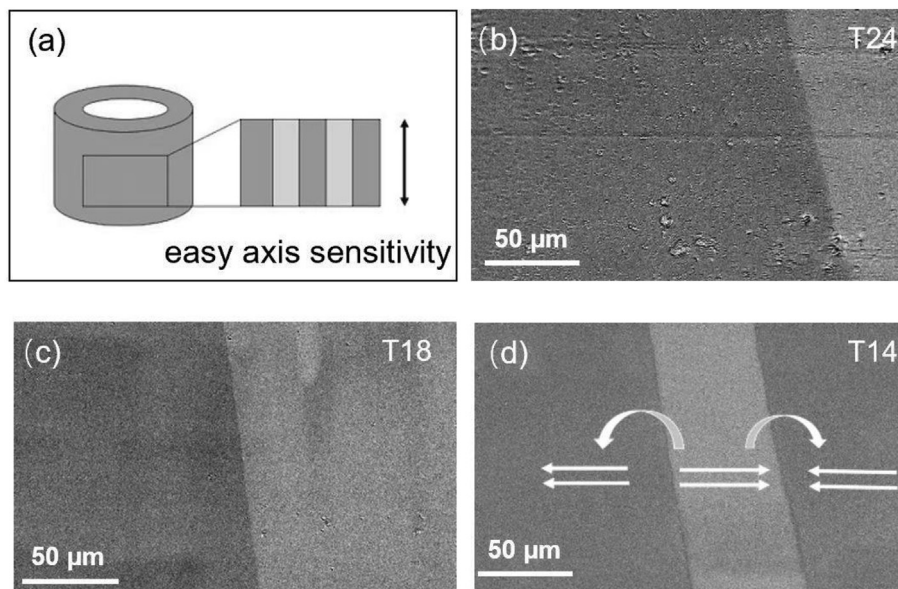

Fig. 8. (a) A schematic map showing the easy axis of the core (b) Magnetic domains at zero magnetic field (i.e. demagnetization state) of the cores.

domains in all the three cores). A larger H_k obviously slows down the increasing rate of the initial magnetization with increasing field. The K_u can be obtained from H_k, and it is found that T24 and T14 have the largest and lowest induced K_u of 5.7 J/m³ and 2.7 J/m³, respectively. Note that these K_u values are comparable to the

theoretically estimated $<K_1>$ ~ 2−4 J/m³ in optimized nano-crystalline Fe-base NAs [16]. The induced anisotropy is generally considered to originate from directional ordering of solute atoms, such as directional ordering of the nearest/next-nearest silicon pairs in α-Fe [39]. And K_u is sensitive to the composition, local
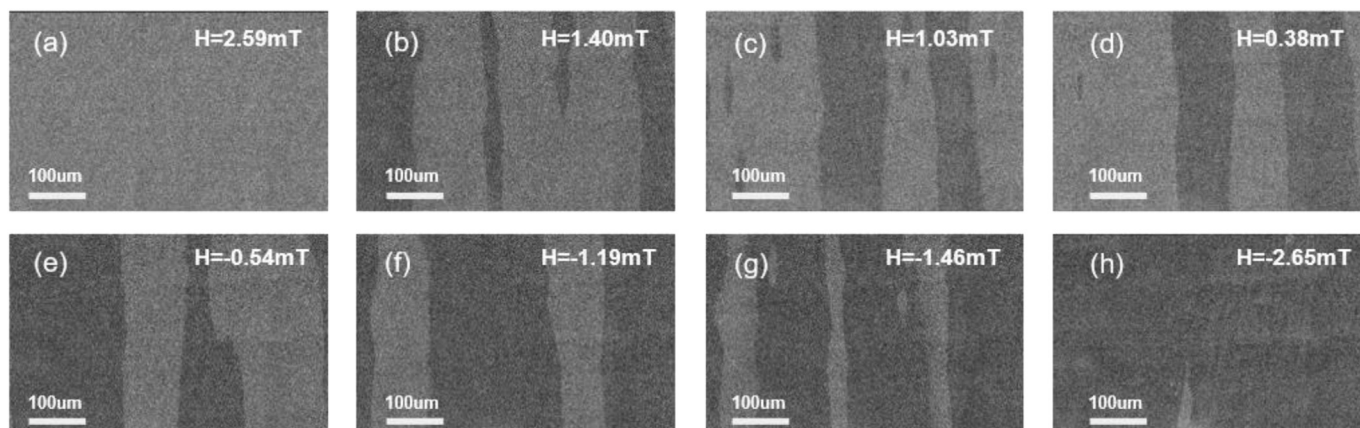
Fig. 9. In situ magnetic domain under a varying static magnetic field for T24.
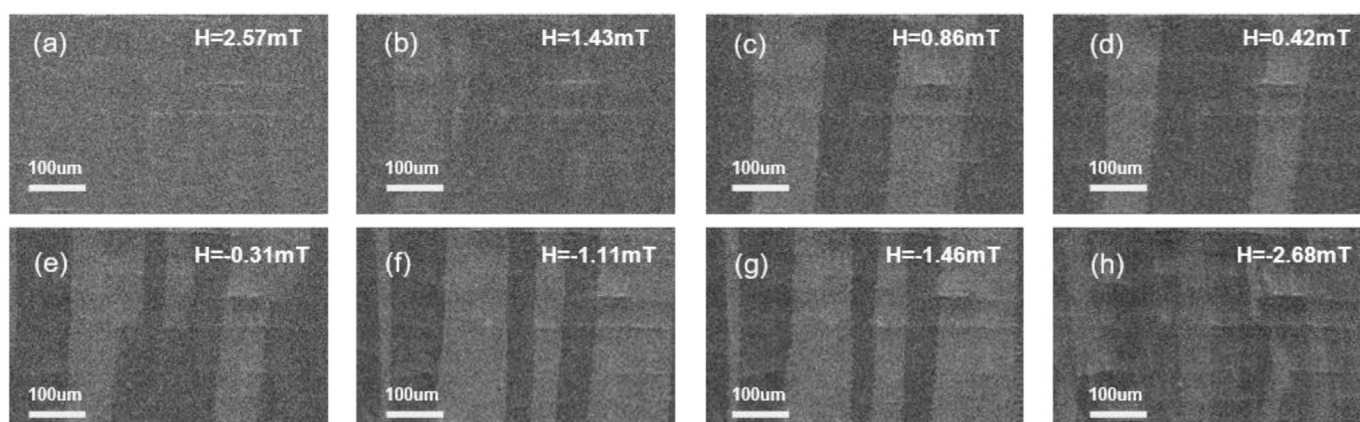

Fig. 10. In situ magnetic domain under a varying static magnetic field for T18.
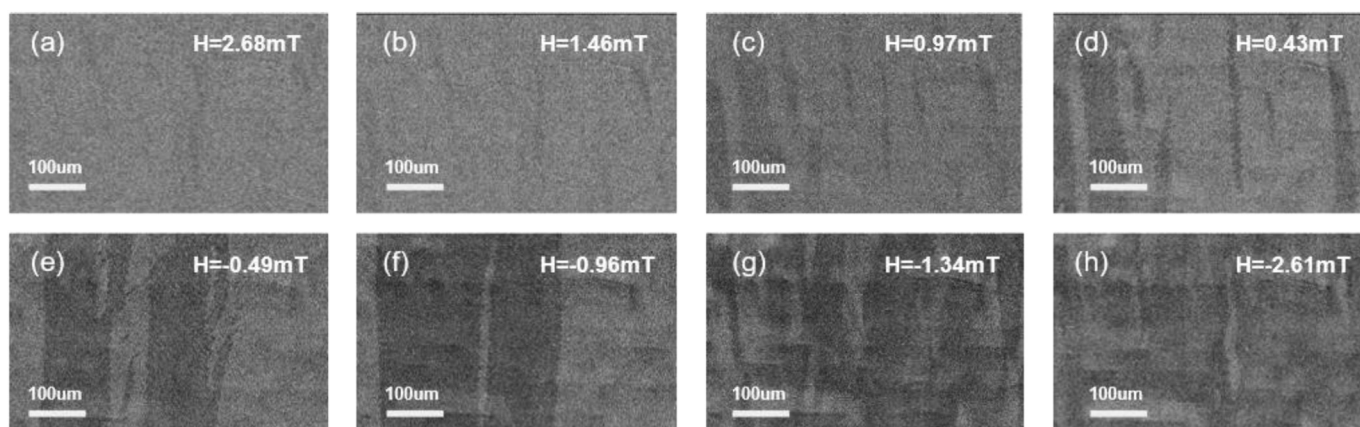

Fig. 11. In situ magnetic domain under a varying static magnetic field for T14.

structure configuration around Fe atoms, and ribbon thickness [39,40]. Thus, the lowest K_u in T14 may be associated with its unique microstructure with the finest α-Fe nanocrystalline grains and its thinnest ribbon thickness.

Now we attempt to rationalize the differences of the static and dynamic domains among the three cores in term of the ribbon thickness, strength of K_u, and especially the interplay between K_u and δK. It is worth noting that, in the case of weak K_u, the δK may

play the same important role as K_u, as evidenced from the observation of irregular magnetization patches within the wide slab domains in the $Fe_{73}Cu_1Nb_3Si_{16}B_7$ NA with a weak K_u ~3 J/m^3 [36]. Another experimental evidence is that the NA with the weakest induced anisotropy had the smallest domain width [36,37], which is different from the case of NAs with large K_u [41]. Based on minimum magnetic Gibbs free energy after considering the anisotropy energy and domain-wall energy [37,42], the domain
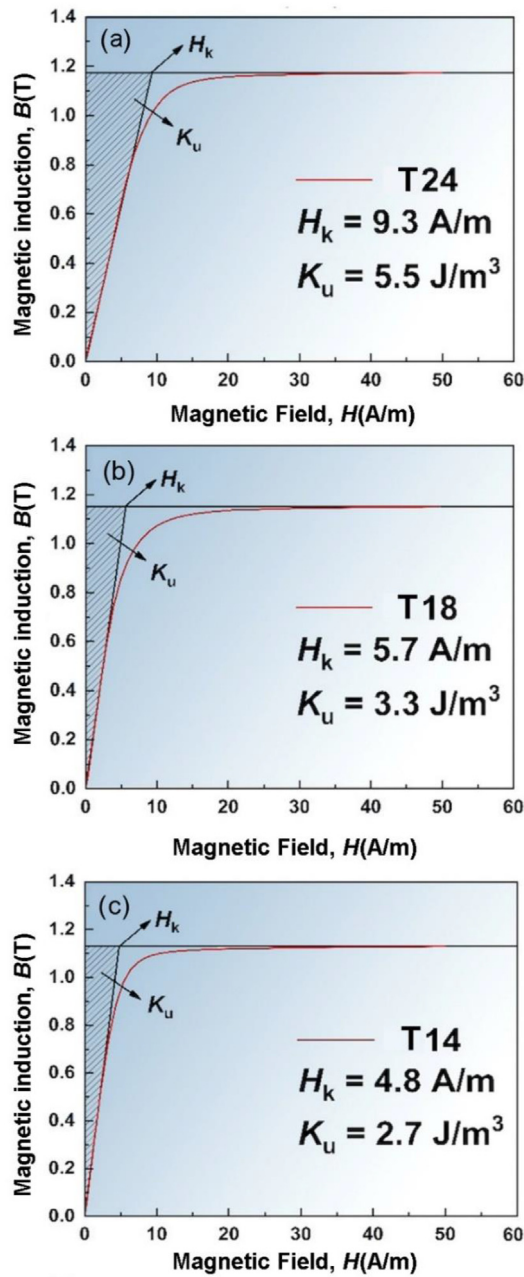
Fig. 12. Initial magnetization curves of the cores, and H_k denotes anisotropy field.

wall width (d) can be expressed as follows: $d \propto t^{1/2}(A/K_u)^{1/4}$, where t, A are the thickness and exchange constant, respectively. Thus, the narrowest magnetic domain width in the demagnetization state of T14 is associated with its thinnest ribbon thickness and weakest K_u, and can be understood. In the dynamic case, the most complicated evolution of domain patterns with the appearance of highest density of narrow strip domains and branches in T14 is due to the strong interplay between the δK and its weakest K_u. The weakest K_u implies the largest angular dispersion of the easiest axis of the local K_1 from one region of exchange coupled grains to another, leading to the most inhomogeneous distribution of the δK among the three cores. In other words, the smaller the K_u is, a more significant role the random anisotropy plays on the domain's evolution, and more splitting and inhomogeneous rotation of the domains during magnetization the core will show. In contrast, T24 with the strongest K_u shows the most homogeneous magnetization process.

The lowest K_u and related highest density of narrow strip domains during demagnetization/magnetization imply that the domain refinement with increasing frequency may be strongest in T14 [36,37]. In the $Fe_{73}Cu_1Nb_3Si_{16}B_7$ cores with different strengths of K_u, it was also found that the core with the weakest K_u shows the strongest wall multiplication, leading to the largest number of domain walls at 10 kHz and its smallest excess loss [36,37]. Accordingly, the strongest wall multiplication with increasing frequency and the largest number of domain walls at 100 kHz can be expected in the T14 core with the lowest K_u. This can largely reduce the wall velocity and lead to its lowest P_{ex}, with 86 kW/m^3 at 100 kHz of T14 in term of theoretical models [32]. Besides, Herzer's theory also implies that a small average domain width conduces to a smaller total eddy current loss for a given thickness [38], in accordance with the present results. Then, a short discussion is given about the permeability at 100 Hz of the cores. According to Herzer's random anisotropy model [9], the T14 sample has the smallest averaged magneto-crystalline anisotropy $<K_1>$ due to its finest grains. And the overall average anisotropy $<K>$ of present samples with comparable K_u and $<K_1>$ can be estimated from $[<K_1>^2+\beta^2K_u^2]^{1/2}$, where parameter β is an anisotropy constant taking different values for different symmetries [9]. And thus, it can be deduced that the T14 sample has the smallest overall average anisotropy constant $<K>$ due to its smallest K_u and $<K_1>$, and correspondingly the highest μ_r, since permeability of NAs is inversely proportional to $<K>$ [9,39].

Fig. 13 presents a schematic diagram summarizing our investigations. Benefiting from the improved cooling strategy of mainly applying a copper roller with the lowest thermal conductivity (Fig. 13(a)), the as-quenched AA ribbon with 14 μm in thickness was prepared with the lowest cooling rate (slowest variation of viscosity η with time or temperature). The T14 AA ribbon contains a larger fraction of crystal-like local order (Fig. 13(b)), which impedes the growth of nanocrystals upon subsequent TFA (Fig. 13(c)). Accordingly, the finest grains are obtained in T14, which along with the size effect results in its largest electrical resistivity. In addition, TFA regulates the domain structure (Fig. 13(d)) and produces the lowest induced anisotropy in T14. Finally, outstanding soft-magnetic performances with μ_r of 48,000 at the condition of 1 A/m and 100 kHz and an ultralow core loss of 94 kW/m^3 at the condition of 0.2 T and 100 kHz are achieved in the T14 core. These values far exceed those of the commercial and experimental NAs reported. The ultralow core loss in the T14 core is mainly ascribed to the ultrathin thickness of the ribbon, finest gains, lowest K_u, and thus strongest competition between K_u and residual random anisotropy, largest electrical resistivity (Fig. 13(e)), all of which jointly promote the formation of a larger number of active domain walls and decrease the eddy current. The ultrathin NAs with exceptional high-frequency performances could further promote and extend the wide high-efficiency and energy-saving applications of NAs in common mode choke, high-frequency transformers, pulse transformers, current sensors, wireless charging, DC/DC-converter in automotive electronics, and so on.
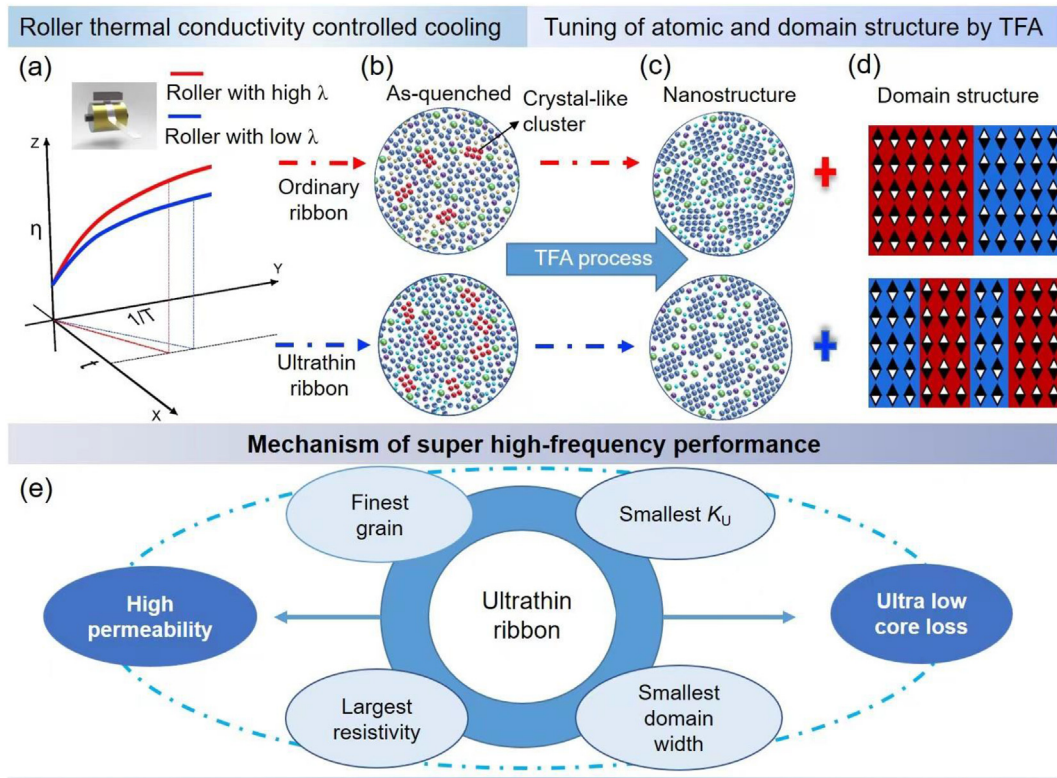
Author contributions

Fig. 13. Schematic diagrams of (a) a cooling process controlled mainly by the thermal conductivity (λ) of the roller, (b) microstructures of the as-quenched ordinary and ultrathin amorphous ribbons, (c) nanostructure and (d) domain structure of the transverse field annealing -treated samples, (e) mechanisms of super high-frequency performance of the ultrathin NA.

and writing-review & editing. All authors contributed to the general discussion.

Declaration of competing interest

The authors declare that they have no known competing financial interests or personal relationships that could have appeared to influence the work reported in this paper.

Data availability

Data will be made available on request.

References

[1] J.M. Silveyra, E. Ferrara, D.L. Huber, T.C. Monson, Soft magnetic materials for a sustainable and electrified world, Science 362 (2018), eaao0195, https://doi.org/10.1126/science.aao0195.

[2] X.H. Li, L. Lou, W.P. Song, G.W. Huang, F.C. Hou, Q. Zhang, H.T. Zhang, J.W. Xiao, B. Wen, X.Y. Zhang, Novel bimorph logical anisotropic bulk nanocomposite materials with high energy products, Adv. Mater. 29 (2017), 1606430, https://doi.org/10.1002/adma.201606430.

[3] A.D. Setyawan, K. Takenaka, P. Sharma, M. Nishijima, N. Nishiyama, A. Makino, Magnetic properties of 120-mm wide ribbons of high B_s and low core-loss NANOMET (R) alloy, J. Appl. Phys. 17 (2015) 5367, https://doi.org/10.1063/1.4913936.

[4] W.C. Li, H.W. Cai, Y. Kang, Y. Ying, J. Yu, J.W. Zheng, L. Qiao, Y. Jiang, S.L. Che, High permeability and low loss bioinspired soft magnetic composites with nacre-like structure for high frequency applications, Acta Mater. 17 (2019) 267–274, https://doi.org/10.1016/j.actamat.2019.01.035.

[5] K. Suzuki, A. Makino, A. Inoue, T. Masumoto, Soft magnetic properties of nanocrystalline bcc Fe-Zr-B and Fe-M-B-Cu (M=transition metal) alloys with high saturation magnetization (invited), J. Appl. Phys. 70 (1991) 6232–6237, https://doi.org/10.1063/1.350006.

[6] A.M. Leary, P.R. Ohodnicki, M.E. McHenry, Soft magnetic materials in high-frequency, high-power conversion applications, JOM 64 (2012) 772–781, https://doi.org/10.1007/s11837-012-0350-0.

[7] Y. Yoshizawa, S. Oguma, K. Yamauchi, New Fe-based soft magnetic alloys composed of ultrafine grain structure, J. Appl. Phys. 64 (1988) 6044–6046, https://doi.org/10.1063/1.342149.

[8] Y. Cao, F.Y. Yang, J.W. Li, A.N. He, A.D. Wang, H.Y. Xiao, Y.Q. Dong, X.C. Liu, B.J. Zhang, Y. Han, High-frequency magnetic characteristics and operating thermal stability of industrialized $Fe_{76}Si_{13}B_8Nb_2Cu_1$ nanocrystalline alloy, J. Magn. Magn Mater. 526 (2021), 167691, https://doi.org/10.1016/j.jmmm.2020.167691.

[9] G. Herzer, Modern soft magnets: amorphous and nanocrystalline materials, Acta Mater. 61 (2013) 718–734, https://doi.org/10.1016/j.actamat.2012.10.040.

[10] K. Hono, D.H. Ping, M. Ohnuma, H. Onodera, Cu clustering and Si partitioning in the early crystallization stage of an $Fe_{73.5}Si_{13.5}B_9Nb_3Cu_1$ amorphous alloy, Acta Mater. 47 (1999) 997–1006, https://doi.org/10.1016/S1359-6454(98)00392-9.

[11] T.-J. Zhou, Z. Yu, Y.W. Du, The effective magnetic anisotropy in nanocrystalline $Fe_{100-x}Si_x$ alloys, J. Magn. Magn Mater. 202 (1999) 354–358, https://doi.org/10.1016/S0304-8853(99)00384-4.

[12] M.A. Willard, D.E. Laughlin, M.E. McHenry, Structure and magnetic properties of $(Fe_{0.5}Co_{0.5})_{88}Zr_7B_4Cu_1$ nanocrystalline alloys, J. Appl. Phys. 84 (1998) 6773–6777, https://doi.org/10.1063/1.369007.

[13] A. Makino, H. Men, T. Kubota, K. Yubuta, A. Inoue, FeSiBPCu nanocrystalline soft magnetic alloys with high B_s of 1.9 tesla produced by crystallizing hetero-amorphous phase, Mater. Trans. 50 (2009) 204–209, https://doi.org/10.2320/matertrans.MER2008306.

[14] E. Lopatina, I. Soldatov, V. Budinsky, M. Marsilius, L. Schultz, G. Herzer, R. Schaefer, Surface crystallization and magnetic properties of $Fe_{84.3}Cu_{0.7}Si_4B_8P_3$ soft magnetic ribbons, Acta Mater. 96 (2015) 10–17, https://doi.org/10.1016/j.actamat.2015.05.051.

[15] X.J. Jia, W. Zhang, Y.Q. Dong, J.W. Li, A.N. He, J.H. Luan, R.W. Li, Unusual alloying effects of Co and Ni on structure and magnetic properties of Fe-Si-B-Cu nanocrystalline alloys with pre-existing α-Fe nanocrystals, J. Alloys Compd. 920 (2022), 166030, https://doi.org/10.1016/j.jallcom.2022.166030.

[16] S. Flohrer, R. Schafer, C. Polak, Interplay of uniform and random anisotropy in nanocrystalline soft magnetic alloys, Acta Mater. 53 (2005) 2937–2942, https://doi.org/10.1016/j.actamat.2005.03.008.

[17] J. Xu, Y.Z. Yang, Q.S. Yan, G.H. Xiao, T. Luo, C.F. Fan, Softening and magnetic properties of ultrahigh Fe content FeSiBCuPC nanocrystalline alloy induced by low-pressure stress annealing, Scripta Mater. 179 (2020) 6–11, https://doi.org/10.1016/j.scriptamat.2019.12.042.

[18] M.A. Willard, M. Daniil, Nanocrystalline soft magnetic alloys two decades of progress, Handb. Magn. Mater. 21 (2013) 173–342, https://doi.org/10.1016/B978-0-444-59593-5.00004-0.

[19] I. Škorvánek, J. Marcin, J. Kováč, Tuning of soft magnetic properties in FeCo- and FeNi-based amorphous and nanocrystalline alloys by thermal process-ing in external magnetic field, Mater. Sci. Forum 783 (2014) 1937–1942, https://doi.org/10.4028/www.scientific.net/MSF.783-786.1937.

[20] https://vacuumschmelze.com/03_Documents/Brochures/PHT%20001%20en.pdf.

[21] https://www.magnetec.de/wp-content/uploads/2021/02/M-019.pdf.

[22] M. Hitachi, Nanocrystalline soft magnetic material "FINEMET". http://www.hitachi-metals.co.jp/e/products/elec/tel/p02_21.html, 2016.

[23] Y. Yoshizawa, K. Yamauchi, Induced magnetic anisotropy and thickness dependence of magnetic properties in nanocrystalline alloy "Finemet", IEEE T. Magn. 5 (1990) 1070–1076, https://doi.org/10.1109/TJMJ.1990.4564397.

[24] B.B. Xing, M. Nie, Q. Zhang, Y.C. Li, Mn-Zn ferrite TP4K material with low power loss at high temperature, Appl. Mech. Mater. 320 (2013) 119–122, https://doi.org/10.4028/www.scientific.net/AMM.320.119.

[25] S. Gotoh, K. Ikeda, T. Otake, A new low loss MnZn ferrite designed to use in the high temperature range above 100°C, J. Jpn. Soc. Powder Metall. 61 (2014) S234–S237, https://doi.org/10.2497/jjspm.61.S234.

[26] F. Mazaleyrat, R. Barruë, Chapter 3 — soft amorphous and nanocrystalline magnetic materials, in: H. Singh Nalwa (Ed.), Handbook of Advanced Elec-tronic and Photonic Materials and Devices, Academic Press, Burlington, 2001, pp. 59–102.

[27] K. Suzuki, A. Makino, A. Inoue, Low core losses of nanocrystalline Fe—M—B (M=Zr, Hf, or Nb) alloys, J. Appl. Phys. 74 (1993) 3316–3322, https://doi.org/10.1063/1.354555.

[28] Y. Yoshizawa, S. Fujii, D.H. Ping, M. Ohnuma, K. Hono, Magnetic properties of nanocrystalline FeMCuNbSiB alloys (M: Co, Ni), Scripta Mater. 48 (2003) 863–868, https://doi.org/10.1016/S1359-6462(02)00611-5.

[29] Y. Yoshizawa, S. Fujii, D.H. Ping, M. Ohnuma, K. Hono, Magnetic properties of nanocrystalline FeCoCuMSiB alloys (M: Nb, Zr), Mater. Sci. Eng. A 375–377 (2004) 207–212, https://doi.org/10.1016/j.msea.2003.10.227.

[30] Q. Wang, C.T. Liu, Y. Yang, J.B. Liu, Y.D. Dong, J. Lu, The atomic-scale mecha-nism for the enhanced glass-forming-ability of a Cu-Zr based bulk metallic glass with minor element additions, Sci. Rep. 4 (2014) 4648, https://doi.org/10.1038/srep04648.

[31] L. Xue, L.L. Shao, Q. Luo, Liquid dynamic and glass formation of $Gd_{55}Co_{20}Al_{25}$ metallic glass with minor Si addition, J. Mater. Sci. Technol. 77 (2021) 28–37, https://doi.org/10.1016/j.jmst.2020.11.024.

[32] G. Bertotti, F. Fiorillo, P. Mazzetti, Basic principles of magnetization processes and origin of losses in soft magnetic materials, J. Magn. Magn Mater. 112 (1992) 146–149, https://doi.org/10.1016/0304-8853(92)91137-I.

[33] J. Füzerová, J. Füzer, P. Kollár, R. Bures, M. Fáberová, Complex permeability and core loss of soft magnetic Fe-based nanocrystalline powder cores, J. Magn. Magn Mater. 345 (2013) 77–81, https://doi.org/10.1016/j.jmmm.2013.06.008.

[34] M.A. Willard, T. Francavilla, V.G. Harris, Core-loss analysis of an (Fe, Co, Ni)-based nanocrystalline soft magnetic alloy, J. Appl. Phys. 97 (2005) 10F502, https://doi.org/10.1063/1.1847333.

[35] Z. Li, K.F. Yao, D.R. Li, X.J. Ni, Z.C. Lu, Core loss analysis of Finemet type nanocrystalline alloy ribbon with different thickness, Prog. Nat. Sci. 27 (2017) 588–592, https://doi.org/10.1016/j.pnsc.2017.09.002.

[36] S. Flohrer, R. Schafer, J. McCord, S. Roth, L. Schultz, G. Herzer, Magnetization loss and domain refinement in nanocrystalline tape wound cores, Acta Mater. 54 (2006) 3253–3259, https://doi.org/10.1016/j.actamat.2006.03.011.

[37] S. Flohrer, R. Schafer, J. McCord, S. Roth, L. Schultz, F. Fiorillo, W. Günther, G. Herzer, Dynamic magnetization process of nanocrystalline tape wound cores with transverse field-induced anisotropy, Acta Mater. 54 (2006) 4693–4698, https://doi.org/10.1016/j.actamat.2006.04.040.

[38] G. Herzer, Magnetic materials for electronic article surveillance, J. Magn. Magn Mater. 254–255 (2003) 598–602, https://doi.org/10.1016/S0304-8853(02)00930-7.

[39] G. Herzer, Anisotropies in soft magnetic nanocrystalline alloys, J. Magn. Magn Mater. 294 (2005) 99–106, https://doi.org/10.1016/j.jmmm.2005.03.020.

[40] H. Fujimori, Chapter 16 — magnetic anisotropy, Amorph. Metall. Alloys (1983) 300–316.

[41] R.H. Zhang, A.N. He, L. Xie, J.H. Zhang, Y.Q. Dong, J.W. Li, B.J. Zhang, Y.X. Liu, Correlation between dynamic magnetization process and dynamic domains of high saturation induction FeSiBNbCuMo nanocrystalline alloy with dual an-isotropies, J. Alloys Compd. 891 (2022), 161956, https://doi.org/10.1016/j.jallcom.2021.161956.

[42] S. Chikazumi, Physics of Ferromagnetism, Clarendon Press, Oxford, 1997.